AFRL-AFOSR-VA-TR-2024-0148

Non-equilibrium plasma interactions with liquid water surfaces

DANIEL LACKS
CASE WESTERN RESERVE UNIV CLEVELAND OH
10900 EUCLID AVE
CLEVELAND, OH,
US

02/09/2024
Final Technical Report

Air Force Research Laboratory
Air Force Office of Scientific Research
Arlington, Virginia 22203
Air Force Materiel Command

REPORT DOCUMENTATION PAGE

PLEASE DO NOT RETURN YOUR FORM TO THE ABOVE ORGANIZATION.

1. REPORT DATE	2. REPORT TYPE	3. DATES COVERED	
20240209	Final	START DATE 20190401	END DATE 20220331

4. TITLE AND SUBTITLE
Non-equilibrium plasma interactions with liquid water surfaces

5a. CONTRACT NUMBER	5b. GRANT NUMBER	5c. PROGRAM ELEMENT NUMBER
	FA9550-19-1-0088	61102F
5d. PROJECT NUMBER	**5e. TASK NUMBER**	**5f. WORK UNIT NUMBER**

6. AUTHOR(S)
Daniel Lacks, R Mohan Sankaran

7. PERFORMING ORGANIZATION NAME(S) AND ADDRESS(ES)
CASE WESTERN RESERVE UNIV CLEVELAND OH
10900 EUCLID AVE
CLEVELAND, OH
US

8. PERFORMING ORGANIZATION REPORT NUMBER

9. SPONSORING/MONITORING AGENCY NAME(S) AND ADDRESS(ES)	10. SPONSOR/MONITOR'S ACRONYM(S)	11. SPONSOR/MONITOR'S REPORT NUMBER(S)
Air Force Office of Scientific Research 875 N. Randolph St. Room 3112 Arlington, VA 22203	AFRL/AFOSR RTB1	AFRL-AFOSR-VA-TR-2024-0148

12. DISTRIBUTION/AVAILABILITY STATEMENT
A Distribution Unlimited: PB Public Release

13. SUPPLEMENTARY NOTES

14. ABSTRACT
The major activities in this project included (i) development of a plasma-droplet reactor and application to nitrogen fixation, (ii) application of ion mobility spectrometry to characterization of plasma-droplet reactions, (iii) development of in-situ diagnostics to measure temperature near a plasma-liquid interface, (iv) development of a model for reaction and transport at the interface of a plasma and liquid water bath, (v) development of a multiscale model to predict species densities at the interface of a plasma and liquid water, and (vi) development of a model for charge decay in the afterglow of a plasma. Significant results or key outcomes and major findings for each of these activities are detailed below.
Plasma-droplet reactor and application to nitrogen fixation. Plasma-liquid processes are generally limited to the contact area between the plasma and the liquid surface. Using liquid microdroplets instead of bulk water can increase the surface to volume ratio and allow the liquid to be full dispersed inside the plasma.

15. SUBJECT TERMS

16. SECURITY CLASSIFICATION OF:			17. LIMITATION OF ABSTRACT	18. NUMBER OF PAGES
a. REPORT U	b. ABSTRACT U	c. THIS PAGE U	UU	19

19a. NAME OF RESPONSIBLE PERSON	19b. PHONE NUMBER *(Include area code)*
ALI SAYIR	426-7236

Standard Form 298 (Rev.5/2020)
Prescribed by ANSI Std. Z39.18

Non-equilibrium plasma interactions with liquid water surfaces

FA9550-19-1-0088

Final Performance Report
April 1st, 2019 – March 31st, 2023

Daniel J. Lacks (PI)
Department of Chemical and Biomolecular Engineering
Case Western Reserve University, Cleveland, OH 44106

R. Mohan Sankaran (Co-PI)*
Department of Nuclear, Plasma, and Radiological Engineering
University of Illinois at Urbana-Champaign, Champaign, IL 61822

*Formerly in Department of Chemical and Biomolecular Engineering, Case Western Reserve University, Cleveland OH 44106

Accomplishments

Research Objectives

The overarching goal of this research project is to understand the nature of interactions between plasmas and liquid water surfaces. Specifically, the project has the following objectives:

1. Study plasma-liquid interactions for different surface-to-volume ratios of the liquid phase.
2. Develop in-situ diagnostics to quantify the effects of plasma-liquid water interactions on the liquid phase.
3. Develop in-situ diagnostics to quantify the effects of plasma-liquid water interactions on the plasma phase.
4. Develop models to support experiments and increase understanding of plasma-liquid water interactions.

Details of Accomplishments

The major activities in this project included (i) development of a plasma-droplet reactor and application to nitrogen fixation, (ii) application of ion mobility spectrometry to characterization of plasma-droplet reactions, (iii) development of in-situ diagnostics to measure temperature near a plasma-liquid interface, (iv) development of a model for reaction and transport at the interface of a plasma and liquid water bath, (v) development of a multiscale model to predict species densities at the interface of a plasma and liquid water, and (vi) development of a model for charge decay in the afterglow of a plasma. Significant results or key outcomes and major findings for each of these activities are detailed below.

Plasma-droplet reactor and application to nitrogen fixation. Plasma-liquid processes are generally limited to the contact area between the plasma and the liquid surface. Using liquid microdroplets instead of bulk water can increase the surface to volume ratio and allow the liquid to be full dispersed inside the plasma.

We have developed a continuous, liquid water droplet plasma system. A schematic of the experimental setup is shown in Fig. 1. The liquid water droplets were generated by atomization and introduced into an atmospheric-pressure dielectric barrier discharge. The droplets were approximately 1 mm in diameter. With argon as the plasma supply gas, the droplets were found to be stable. With nitrogen as the plasma supply gas, the droplets were completely evaporated at the exit of the reactor. The gas temperatures for both plasmas were somewhat similar, but we found that the nitrogen plasma was much more filamentary, suggesting that filaments were responsible for breaking up and/or heating the droplets.

The plasma-water droplet reactor was applied to nitrogen fixation. After performing control experiments, the production of various forms of fixed nitrogen including ammonia, nitrate, and nitrite was characterized, as shown in Fig. 2. The reaction between nitrogen and water is complex because there is simultaneous reduction to ammonia, and oxidation to nitrate and nitrite. By carrying out a systematic set of experiments with different feedstocks, we showed, not so surprisingly, that ammonia was formed from hydrogen radicals created from water, and nitrate and

nitrite were formed from hydroxyl radicals created from water. A study reporting these results has been published (J. R. Toth et al., "Plasma-water droplet reactor for process-intensified, continuous nitrogen fixation at atmospheric pressure," *ACS Sustainable Chem. Eng.* **8**, 14845-14854, 2020).

Ion mobility spectrometry to characterize plasma-droplet reactions. Plasma-liquid interactions in both bulk liquid and liquid water droplets have been used to synthesize metal nanoparticles. Nanoparticle synthesis in droplets has been found to exhibit rates greater than other processes and has potential to synthesize materials that do not have volatile precursors. However, there has not been much understanding of the mechanism behind nanoparticle nucleation and growth and the role of the plasma and the liquid-phase chemistry.

We developed online measurements of nanoparticle synthesis in a plasma-droplet reactor using ion mobility spectrometry. This tool has been previously applied to gas-phase synthesis of nanoparticles from vapor precursors, using plasmas, as well as hot wall furnaces. To our knowledge, it has never been applied to nanoparticle synthesis in a plasma-droplet reactor. In our experiments, as illustrated in Fig. 3, water droplets containing silver nitrate were introduced in a dielectric barrier discharge to nucleate and grow silver nanoparticles. Ion mobility spectrometry measured the mobility diameter distribution. Measurements were performed both with the plasma off and on. When the plasma was off, the precursor salt dries and the diameter of this aerosol particle is measured. When the plasma is on, the precursor first reacts inside the droplet with plasma species, and after being converted to metal nanoparticles, the diameter of this aerosol particle is measured. The diameters of the aerosol particles for the two cases are different because of density differences, and were compared to assess the conversion of the precursor to metal. As a control, we also performed laser scattering to obtain the diameter distribution of untreated particles and calculated the diameter distribution for 100% conversion.

Figure 4 shows shifts in the diameter distribution, as predicted by laser scattering (Fig. 4a) and measured by ion mobility spectrometry (Fig. 4b), confirming that the precursor is converted. We then showed that similar shifts in diameter distribution were not observed when the droplets were first dried before being introduced in the plasma. In the absence of liquid water, the dried salt particles could not be converted to metal. These results showed that water is critical, and suggested that through plasma-liquid interactions, some species, such as solvated electrons, is needed to react with the precursor and convert it to metal. A study reporting these results has been published (T. Gallingani et al., "Online ion mobility spectrometry of nanoparticle formation by non-thermal plasma conversion of metal salts in liquid aerosol droplets," *J. Aerosol Sci.* **150**, 105631, 2020).

In-situ diagnostics to measure temperatures. One of the most basic issues for plasma-liquid interactions is the temperature. In the plasma, there are multiple temperatures, with the two most important being the electron temperature and the neutral gas temperature. For the liquid, there is a temperature near the surface and a temperature inside the bulk liquid. All of these temperatures are different and there can be large gradients over small length scales because of the various heating and cooling mechanisms. Practically speaking, the temperatures can be important because a plasma can heat up a liquid and cause evaporation, which will destabilize the interface. For this reason, measuring and controlling the temperature can be critical to any fundamental study or application. However, because of the large temperature gradients and small dimensions which prevent physical probes, measuring the temperature can be challenging.

We have developed an in-situ diagnostic to measure temperature, supported by modeling, to characterize the spatial temperature gradients at a plasma-liquid interface. A schematic of the experimental setup that was the focus of our characterization is shown in Fig. 5. We applied near-infrared (NIR) thermometry to obtain the temperature at the plasma electrode and mid-range infrared thermometry to obtain the temperature at the surface of the liquid (water). We took advantage of blackbody radiation from the electrode and recorded and fit the spectrum. These estimates were supported by optical emission spectroscopy and analysis of the rovibrational lines for OH generated from water vapor.

The results showed somewhat surprisingly that the electrode and the plasma can heat up to temperatures >1000 K, but the surface of the water, despite being only 1 mm away from the electrode tip, remains less than ~320 K. Modeling confirmed that in this geometry, large temperature gradients are created by the highly localized heating and effective heat dissipation at the boundary of the plasma and the liquid bulk. We are now preparing a manuscript for publication.

Reaction and transport at the interface of a plasma and liquid water bath. There are a growing number of applications where a plasma treats a chemical in the liquid phase. The reactions occur at the interface of the plasma and liquid. Because the reaction is usually very fast, treatment of the chemical becomes limited by mass transport of the chemical from the bulk of the liquid to the interface where the reaction occurs.

We developed an analytical model to quantify the relative effect of mass transport on a reaction at a plasma-liquid interface. The focus of this study was the degradation of an organic contaminant in water, perfluorooctanoic acid (PFOA), in the same experimental setup shown in Fig. 1. As shown in Figs. 6a and b, the observed rate for degradation of PFOA exhibited a first order dependence. We suspected that this was not because of the kinetics, but rather because of mass transport effects. The simplest model for combined mass transfer and chemical kinetics relevant to our system is a film model. Assuming first-order kinetics, the film model yields the following expression for degradation efficiency:

$$\frac{X_{D,1}}{100} = 1 - \exp\left(-\frac{A_s}{V_{liq}} \frac{k_{r,1}}{1 + k_{r,1}/k_m} t \right) \tag{1}$$

where $X_{D,1}$ is the percentage conversion of PFOA for the first-order reaction, A_s is the interfacial area for treatment, V_{liq} is the liquid bulk volume, $k_{r,1}$ is the intrinsic reaction rate constant for the first-order reaction, k_m is the mass transfer coefficient, and t is time.

From Eq. 1, we can relate the observed rate constant, $k_{obs,1}$, which is measured in experiments to $k_{r,1}$ and k_m:

$$k_{obs,1} = \frac{A_s}{V_{liq}} \frac{k_{r,1}}{1 + k_{r,1} / k_m} \tag{2}$$

To independently determine $k_{r,1}$ and k_m, we need to identify process conditions that can vary the kinetics or mass transfer. Here, we assumed that the reaction of PFOA proceeds via an Eley-Rideal type mechanism where gas-phase electrons directly react with the "adsorbed", solution-phase PFOA molecules. Thus, the reaction depends on the concentration of gas-phase electrons, which by a drift-diffusion model of the plasma can be shown to depend on the discharge current:

$$C_e = \frac{I}{A_s F} \frac{1}{\mu_e / d_a \left(|V_a| + k_B T_e / e \right)} \tag{3}$$

We thus performed experiments at different currents and by fitting the above equations, as shown in Fig. 6c, determined $k_{r,1}$, which in the case of the PFOA reaction was estimated to be ~443 m/s.

The methodology that we developed is the first quantitative model of reaction-transport at a plasma-liquid interface, and could be applied to any reaction at a plasma-liquid interface that follows an Eley-Rideal reaction mechanism. A study reporting these results has recently been published (N. B. Uner et al., "Rate, efficiency, and mechanisms of electrochemical perfluorooctanoic acid degradation with boron-doped diamond and plasma electrodes," *Langmuir* **38**, 8975-8986, 2022).

Multiphase model of reaction and diffusion at the interface of a plasma and liquid water. Extending from the above analytical model of the reaction-transport at a plasma-liquid interface, a multiscale model of the physics and chemistry of plasma-liquid interactions would help support and guide experiments, and eventually provide predictive capabilities. Up to now, such models have lagged behind experiments. A part of the reason is that the interactions at a plasma-liquid interface are very complex, encompassing two different phases (gas and liquid) and transport across the phases.

In collaboration with Prof. Davide Curreli, we developed a one-dimensional, time-dependent, multi-physics model that encompasses the plasma and liquid phases, and the interface. The model was centered around solving drift-diffusion-reaction equations, and simulations were carried out using the MOOSE-based software, Zapdos-Crane. Importantly, the exact same configuration as the experiment setup shown in Fig. 1 was modeled, except that in the model, the simulation domain for the water region was only 10 μm in order to minimize computational time. Briefly, the model of the plasma phase consisted of 32 species and 301 total reactions. The reaction network was largely based on a reduced humid Ar chemistry. Gaseous charged species were allowed to contact the interface with a flux dictated by the transport coefficients and gas-phase densities. Cations were assumed to immediately exchange charge with liquid water. Anions are less understood, and were assumed to enter and become solvated (including electrons). Neutral species were allowed to enter water and their interfacial concentrations were calculated based on Henry's law. The

model of the water phase included 10 ionic species, 9 dissolved neutral species, and 72 reactions.

As a first step towards developing and validating the model, we focused our study on a Ar plasma in contact with water containing NaCl. We compared both a plasma operated as the cathode (negatively biased) and as the anode (positively biased) in an electrochemical-type process. Simulation results for the spatial concentrations of various species in the plasma and liquid phases are shown in Figs. 7a and b, respectively. One of the key differences that the simulations reveal is the much higher concentration of H_2O_2 generated in the liquid phase for the anodic case. Interestingly, H_2O_2 is formed very similarly in the gas phase for both the cathodic and anodic cases. For this reason, we hypothesized that H_2O_2 is initially formed in the gas phase in both cases and dissolves, but in the cathodic case, is degraded. The most likely mechanism for degradation is solvated electrons which are predominantly generated in the cathodic case. The modeling results were supported by experiments that also showed much more H_2O_2 is produced in the anodic case. We further demonstrated by adding a scavenger for solvated electrons, $NaNO_3$, that the H_2O_2 concentration in the cathodic case could be increased, supporting our hypothesis that solvated electrons degrade H_2O_2.

The model that we have developed is the first of its kind to predict plasma and liquid water interactions. The model is applied to understanding differences in formation of H_2O_2 for a cathodic vs. anodic plasma. The model is general and could be applied to other configurations and chemistries in the future. A study reporting these results has been published (S. Keniley *et al.*, "Multiphase modeling of the DC plasma-water interface: Application to hydrogen peroxide generation with experimental validation," *Plasma Sources Sci. Technol.* **31**, 075001, 2022).

Charge decay in the afterglow of a plasma. In many applications, including plasma-liquid processes, the boundary of the plasma interacts with the surface. This region, which connects the bulk plasma with the ambient, is known as the spatial afterglow. There is growing evidence that the properties of the spatial afterglow are distinct from the bulk plasma.

We characterized the spatial afterglow of a plasma and developed a model. A diagnostic chamber was designed as shown in Fig. 8 to make the first direct measurement of the plasma density in the spatial afterglow as a function of distance from the bulk plasma using double Langmuir probe (DLP).

In support of experimental measurements, a one-dimensional advection-diffusion-recombination model was developed. Charged species in the spatial afterglow engage in advection (mediated by the neutral gas), diffusion to the walls and three-body, volume recombination in the spatial afterglow. For an axisymmetric geometry and assuming that quasineutrality holds, our advection-diffusion-reaction model expresses the charged species density in the spatial afterglow as:

$$n(z) = \frac{n_\mathrm{p}}{\left(1 + \frac{k_\mathrm{r} n_\mathrm{g} n_\mathrm{p} \Lambda^2}{2D_\mathrm{a}}\right) \exp\left[\frac{2D_\mathrm{a}}{v_\mathrm{f}\Lambda^2}(z - \gamma_0)\right] - \frac{k_\mathrm{r} n_\mathrm{g} n_\mathrm{p} \Lambda^2}{2D_\mathrm{a}}} \qquad (1)$$

where k_r is the three-body recombination rate constant, n_g is the neutral gas density, Λ is a characteristic diffusion length in the radial direction, and v_f is the fluid velocity and equal to the

volumetric flowrate, Q, divided by the flow cross-sectional area. Computational fluid dynamics suggested that Λ is approximately equal to the tube radius (*i.e.*, negligible jet expansion in the chamber, see Supplementary Note 4 and Supplementary Fig. 7), and, therefore, v_f is approximately equal to the average fluid velocity in the tube. In this formulation, the origin of the z-axis is the ground electrode, and γ_0 is the distance to the bulk plasma-afterglow boundary. All parameters involved in the model can be readily calculated or estimated by using literature data or by utilizing the DLP measurements.

With all parameters of the model defined, we non-dimensionalized the model to consolidate variables into dimensionless groups that determine the structure of the spatial afterglow:

$$\eta(\xi) \equiv \frac{n}{n_p} = \frac{1}{\exp(\xi) + \phi^2[\exp(\xi) - 1]} \tag{2}$$

where ξ is the axial distance in the spatial afterglow, $z - \gamma_0$, normalized to the characteristic decay length, $\lambda_c \equiv (v_f\Lambda^2/2D_a)$, and $\phi \equiv (k_r n_g n_p \Lambda^2/2D_a)^{1/2}$. From Equation 2, we can define ϕ as a Thiele modulus, a well-known dimensionless parameter found in chemical engineering that relates the ratio of the rates of diffusion to reaction. Here, ϕ compares the relative rates of three-body recombination to diffusional loss of charge.

We validated the spatial afterglow model by comparing with experimental measurements. Figure 9a shows that γ_0 obtained from DLP measurements has excellent agreement with calculations based on the power model over all the pressures studied. The forward power was directly measured, but for RF plasmas, it is known to differ, sometimes substantially, from the power absorbed, P_w, which is difficult to assess. For this reason, we assumed P_w to be independent of pressure and was approximated to be the forward power.

We next calculated ϕ as a function of pressure, comparing calculations assuming linear approximation for bulk plasma density and calculations based on exact experimental measurements. The Thiele modulus is quite sensitive to changes in pressure, with a $p^{3/2}$ dependence, and the model and experiment show excellent agreement, as shown in Fig 9b. When $\phi < 1$, diffusive losses dominate the charged species' decay in the spatial afterglow, and when $\phi \geq 1$, three-body recombination becomes prominent. Physically, when the pressure is low, three-body recombination in the volume is limited, and diffusion to the walls is the primary loss mechanism for charged species, and when the pressure is high, three-body recombination is enhanced. These loss mechanisms balance each other when $\phi \approx 1$ at ~150 Torr.

Finally, the dimensionless charge density, η, was calculated as a function of the dimensionless axial distance in the spatial afterglow, ξ, for different values of ϕ and was compared to DLP measurements, where corresponding spatial coordinates for DLP measurements are adjusted by γ_0. As shown in Fig. 9c, at relatively low pressures (< 75 Torr), the decay profile is found to follow an exponential trend and produced excellent agreement with experimental measurements. As the pressure rises, so does the density of neutral gas atoms, thus increasing the volumetric recombination rate, resulting in greater values of ϕ. As shown in Fig. 9c, when $\phi \approx 1$ at 150 Torr,

the decay profile shifts away from an exponential, especially at small distances. At higher pressures (300 Torr), where $\phi \approx 2$, the shift is even more apparent. Model calculations and experimental measurements show good agreement for 300 Torr and moderately so for 150 Torr. Overall, charged species density measurements via DLP provide evidence for the validity of the proposed spatial afterglow model.

The benefit of a working model is that the calculations can be extended to other process conditions, including those challenging for experiments. For example, atmospheric pressure is an important process condition for applications of continuous-flow plasmas. However, we were unable to perform conventional DLP analysis of the afterglow at pressures higher than 300 Torr. Specifically, at 400 Torr, the DLP traces did not exhibit the expected sigmoidal shape corresponding to the electron retardation region, and were instead linear, suggesting a low density of charged species and, in particular, the absence of hot electrons. With our validation of the model at pressures where experimental measurements were possible, we are able to circumvent the experimental challenges faced at higher pressures by extending our model calculations to higher pressures up to atmospheric (~760 Torr).

In an afterglow, the charged species density decreases over time or space, which leads to fundamental changes to our picture of a plasma. It has been previously reported that in a temporal afterglow, the apparent mode of diffusion changes from ambipolar diffusion to free diffusion. The transition between the regimes was defined by a normalized diffusivity, defined as the ratio of the apparent diffusivity to the intrinsic ion diffusivity, D_{app}/D_i, which in turn is a function of the ratio, $\chi \equiv \Lambda/\lambda_D$, defined as the ratio between the characteristic diffusion length, Λ, and the Debye length, λ_D. Here, we applied a similar analysis to a spatial afterglow. We first used our model of the spatial afterglow to express λ_D as a function of axial distance from the bulk plasma:

$$\lambda_D(\xi) = \lambda_{Dp}\sqrt{\exp(\xi) + \phi^2[\exp(\xi) - 1]}, \tag{3}$$

where $\lambda_D = (\epsilon_0 T_e/q_e n_p)^{1/2}$ is the Debye length in the bulk plasma. By solving for the dimensionless distance, ξ, we calculated the normalized apparent diffusivity, D_{app}/D_i, for ions and electrons in the spatial afterglow. At small ξ, *i.e.*, when χ is large (>1000), the normalized diffusivities for ions and electrons coincide and charged species follow ambipolar diffusion. At large ξ, where the charged species density decays to a much lower value, χ decreases, the normalized diffusivities for ions and electrons suddenly deviate (with the latter rapidly increasing and the former rapidly decreasing), and ions and electrons no longer diffuse at similar rates. For ions, the diffusion is completely free of electrostatic effects when D_{app}/D_i is equal to unity, which is achieved at small χ values. We can thus define a critical value for χ of 30, below which ambipolar diffusion no longer holds. This critical value occurs at different distances depending on the operating conditions, but always at the dimensionless distance ξ_{crit}, which can be expressed as:

$$\xi_{crit} = \ln\left[\frac{\left(\chi_p/\chi_{crit}\right)^2 + \phi^2}{1 + \phi^2}\right] \tag{4}$$

The consequence of the transition from ambipolar to free diffusion is that ions and electrons approach their intrinsic diffusivity limits, and because electrons are much more mobile, they are lost from the spatial afterglow faster, leading to regions that are ion-rich and have a positive space charge. Thus, ξ_{crit} demarcates a breakdown of ambipolar diffusion and quasi-neutrality. A study reporting these results has been published (N. Abuyazid *et al.*, "Charge decay in the spatial afterglow of plasmas and its impact on diffusion regimes," *Nat. Comm.* **14**, 6776, 2023).

Publications (overall)

1. J. Beckers et al., "Physics and applications of dusty plasmas: The Perspectives 2023," *Phys. Plasmas* **30**, 120601 (2023).
2. J. Wang, N. B. Uner, S. E. Dubowsky, M. P. Confer, R. Bhargava, Y. Y. Sun, Y. T. Zhou, R. M. Sankaran, and J. S. Moore, "Plasma electrochemistry for carbon-carbon bond formation via pinacol coupling," *J. Am. Chem. Soc.* **145**, 10470-10474 (2023).
3. N. B. Uner, P. B. Medina, J. L. Dinari, X. Su, and R. M. Sankaran, "Rate, efficiency, and mechanisms of electrochemical perfluorooctanoic acid degradation with boron-doped diamond and plasma electrodes," *Langmuir* **38**, 8975-8986 (2022).
4. S. Keniley, N. B. Uner, E. Perez, R. M. Sankaran, and D. Curreli, "Multiphase modeling of the DC plasma-water interface: application to hydrogen peroxide generation with experimental validation," *Plasma Sources Sci. Technol.* **31**, 075001 (2022).
5. D. T. Elg, H. E. Delgado, D. C. Martin, R. M. Sankaran, P. Rumbach, D. M. Bartels, and D. B. Go, "Recent advances in understanding the role of solvated electrons at the plasma-liquid interface of solution-based gas discharges," *Spectrochim. Acta B: At. Spectrosc.* **186**, 106307 (2021).
6. T. Gallingani, N. H. Abuyazid, V. Colombo, M. Gherardi, and R. M. Sankaran, "Online ion mobility spectrometry of nanoparticle formation by non-thermal plasma conversion of metal salts in liquid aerosol droplets," *J. Aerosol Sci.* **150**, 105631 (2020).
7. J. R. Toth, N. H. Abuyazid, D. J. Lacks, J. N. Renner, and R. M. Sankaran, "A plasma-water droplet reactor for process-intensified, continuous nitrogen fixation at atmospheric pressure," *ACS Sustain. Chem. Eng.* **8**, 14845-14854 (2020).
8. J. R. Toth, R. Hawtof, D. Matthiesen, J. N. Renner, and R. M. Sankaran, "On the non-faradaic hydrogen gas evolution from electrolytic reactions at the interface of a cathodic atmospheric-pressure microplasma and liquid water surface," *J. Electrochem. Soc.* **167**, 116504 (2020).

Student/personnel

Joseph Toth – Ph.D. 2020
Nabiel Abuyazid – Ph.D. 2022
Scott Dubowsky – Postdoctoral researcher
Necip Uner – Postdoctoral researcher

Impacts

Our research has revealed fundamental insight into interactions at a plasma and liquid water interface that will enable their applications in a wide-range of technologies. The unique combination of experiments and modeling provides validation and predictive capabilities. Specifically, we have developed an in-situ diagnostic for measuring nanoparticles produced from liquid droplets and measuring temperature at the plasma-liquid interface. We have developed an

analytical model for reaction and transport, a multiphase model that can predict 1D species concentrations near the plasma-liquid interface, and a phenomenological model for charge decay in the spatial afterglow.

The research has involved two graduate students who have both successfully received their Ph.D.'s (Joseph Toth and Nabiel Abuyazid) and one postdoctoral researcher (Dr. Scott Dubowsky). Another postdoctoral researcher was also involved in the work without direct support (Dr. Necip Uner). One undergraduate student (Jasmine Dinari) also participated in the research and received a fellowship from UIUC to support her work. She was recognized with the Outstanding Undergraduate Research Award from the Department of Nuclear, Plasma, and Radiological Engineering for her research contributions.

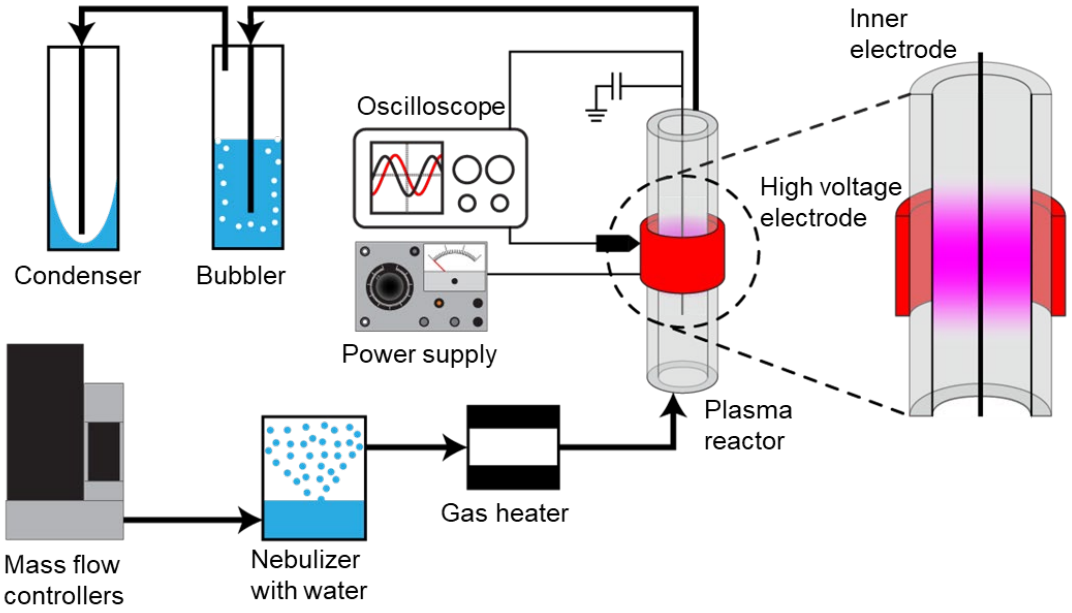

Figure 1. Schematic of continuous, atmospheric-pressure plasma system studied for reaction of nitrogen gas and water droplets.

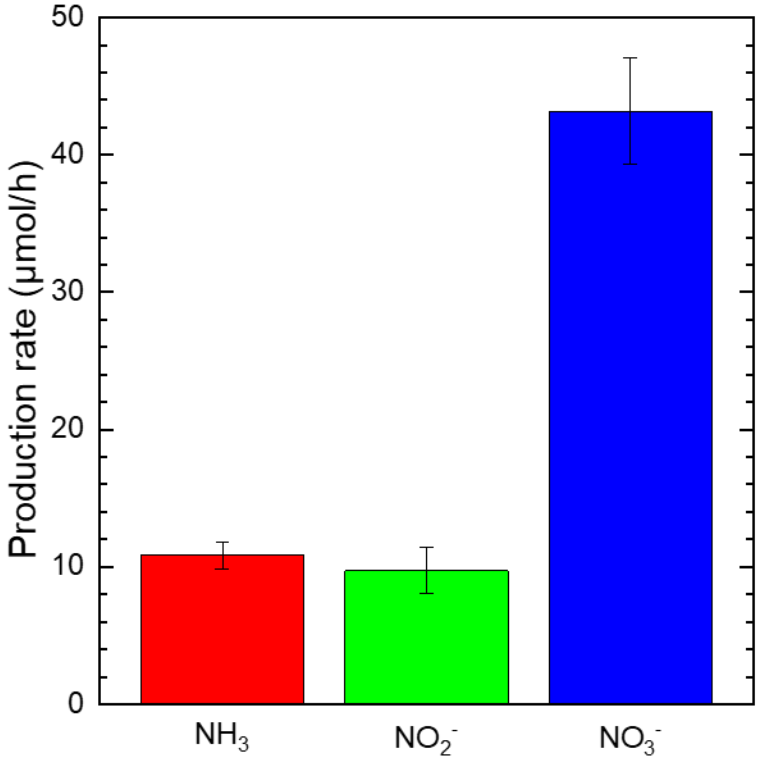

Figure 2. Production rates of NH_3, NO_3^-, and NO_2^- measured in plasma-water droplet reactor operating in nitrogen gas at 24 W.

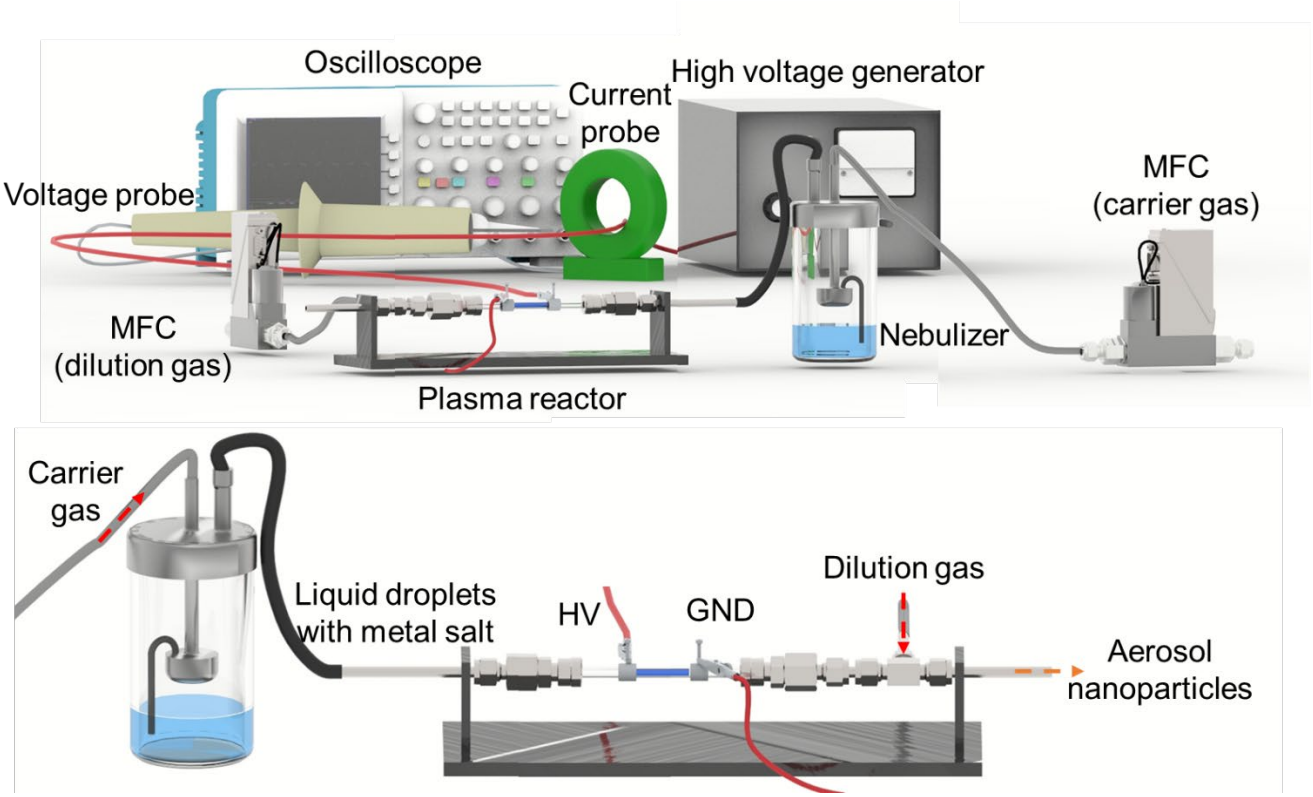

Figure 3. Illustration of the experimental setup consisting of droplet generation by a nebulizer and an atmospheric-pressure DBD for precursor conversion.

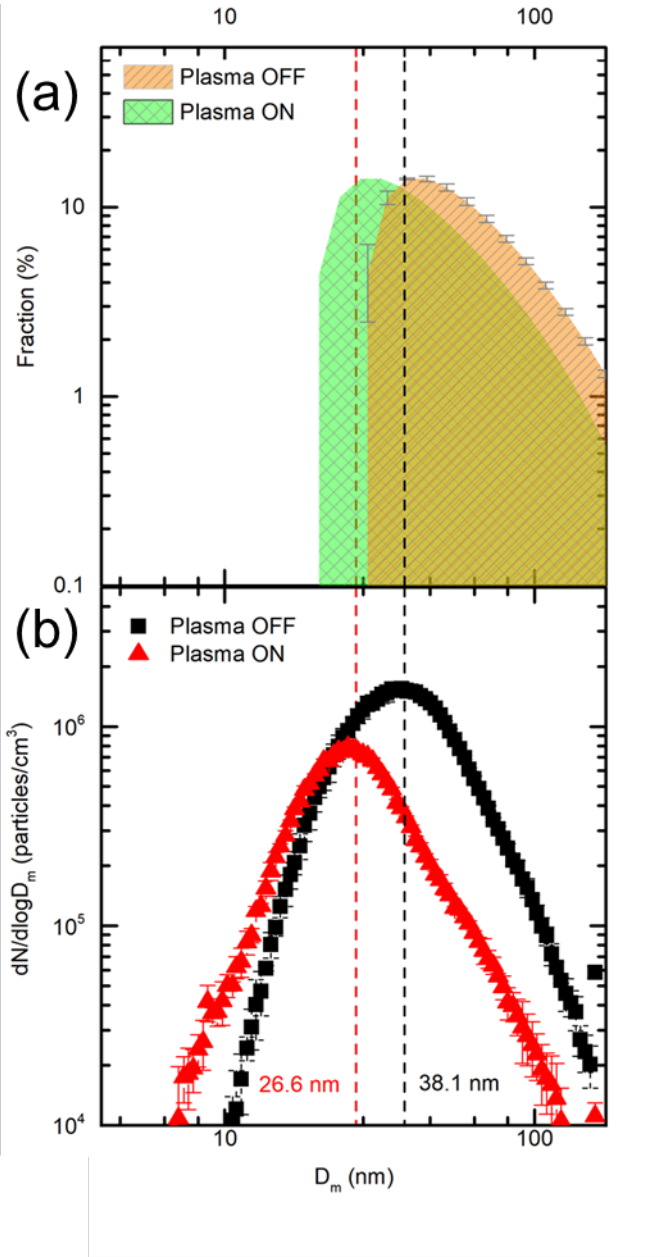

Figure 4. (a) Expected particle size distributions of untreated (orange) based on laser diffraction and treated (green) based on 100% conversion. (b) Mobility diameter distributions measured by ion mobility spectrometry for plasma off (black square) and plasma on (red triangle) cases.

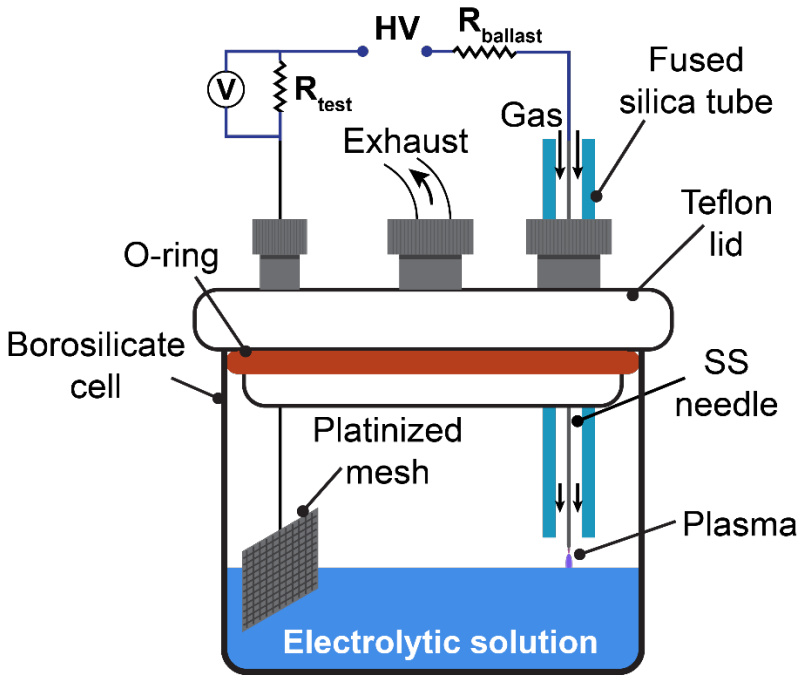

Figure 5. Schematic of DC plasma in an electrolytic setup consisting of a plasma formed between a needle and a liquid water surface, a counter electrode, and a sealed glass cell with feedthroughs for the electrical connections, gas feed, and exhaust.

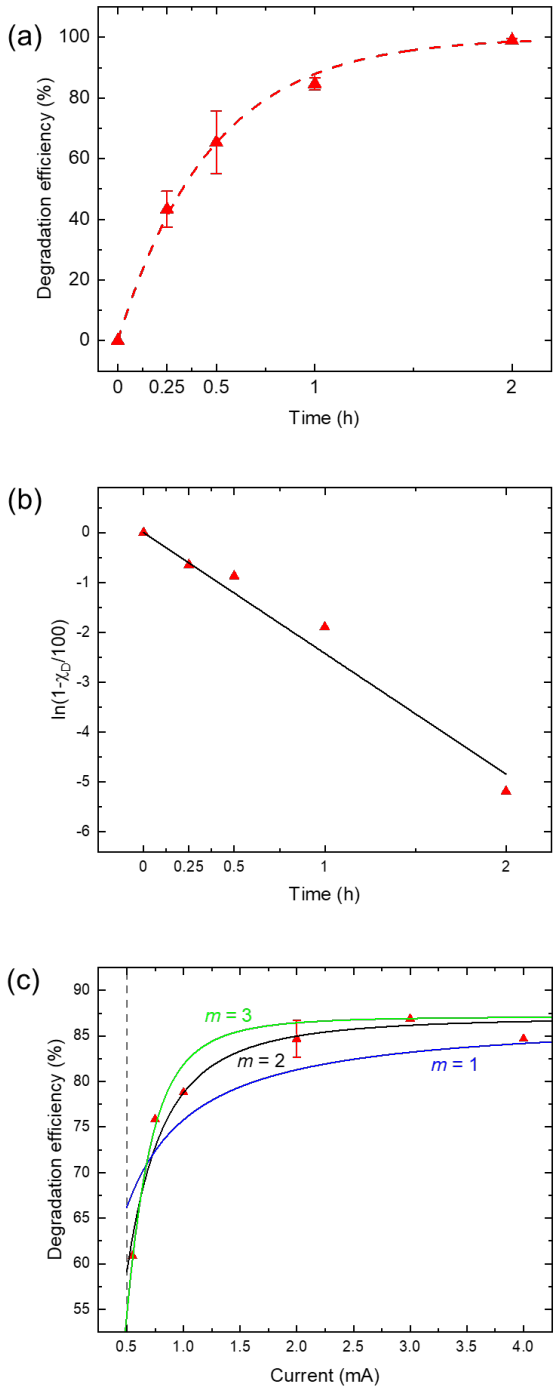

Figure 6. (a) Degradation efficiency of PFOA vs. time by a cathodic DC plasma in an electrolytic setup. (b) Kinetic analysis showing that the observed rate follows a first-order rate dependence. (c) Analysis of degradation efficiency vs. current that allows the intrinsic rate constant to be separated from the mass transfer coefficient.

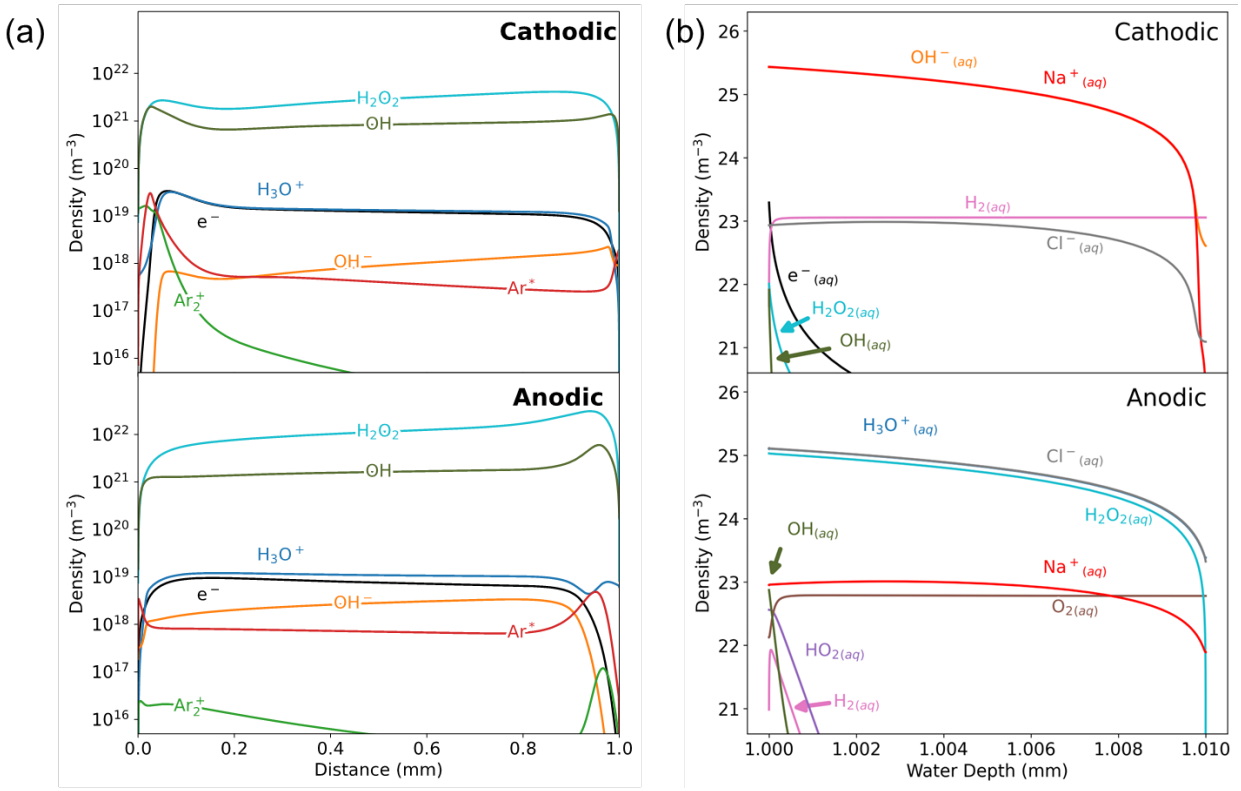

Figure 7. (a) Simulation results for densities of species in the gas phase of a DC Ar plasma in contact with liquid water operated as either the cathode or the anode. The electrode surface is at x= 0 mm and the water surface is at x=1 mm. (b) Simulation results for densities of species in the liquid phase of a DC Ar plasma in contact with liquid water operated as either the cathode or the anode.

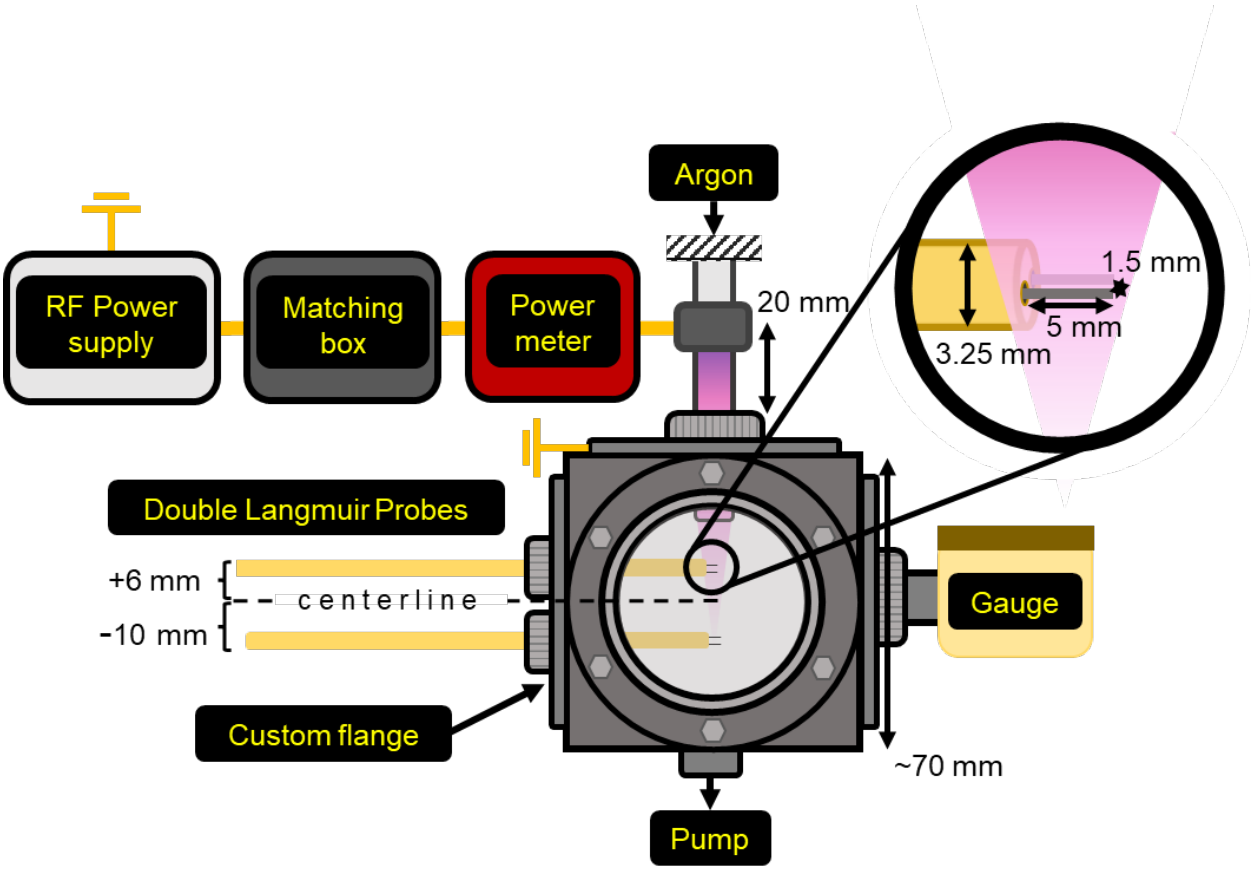

Figure 8. (a) Schematic of experimental setup for generation and characterization of spatial afterglow.

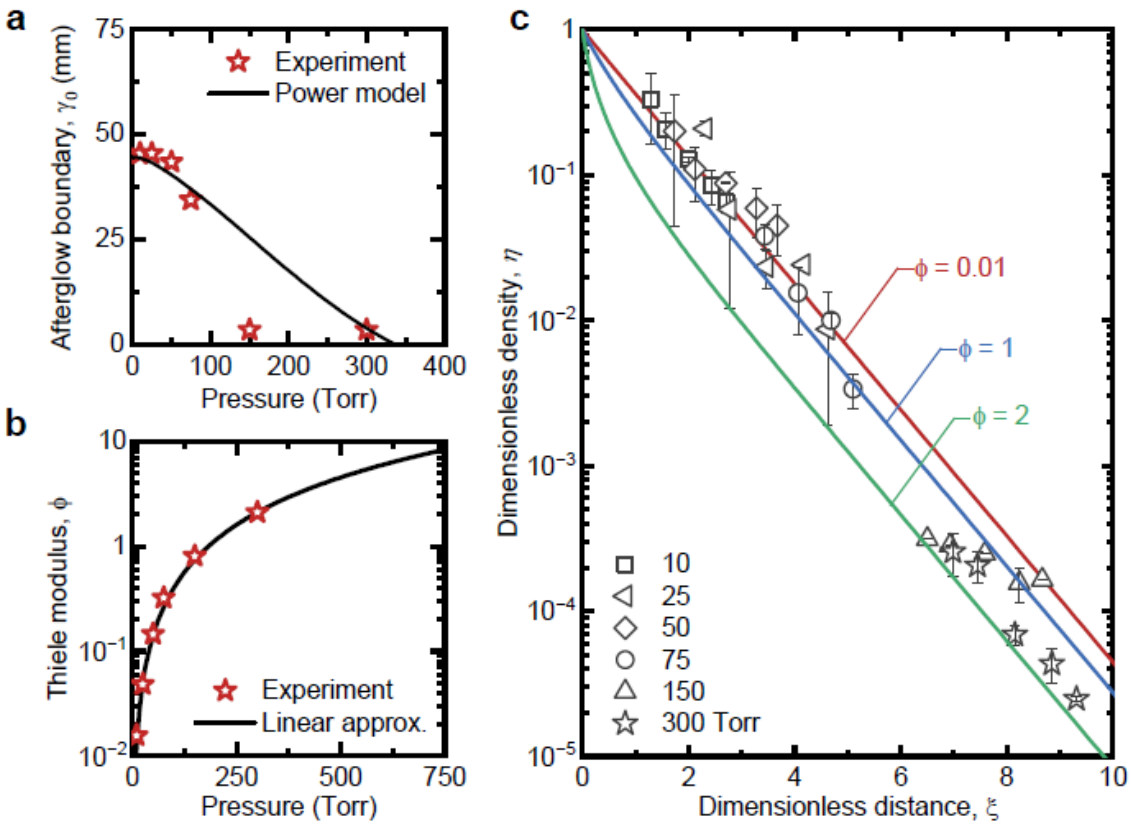

Figure 9. (a) Location of bulk plasma-afterglow boundary as a function of pressure. (b) Thiele modulus as a function of pressure. (c) Dimensionless charge density as a function of dimensionless axial distance in the spatial afterglow.